CO$_2$ Hydrogenation on Unpromoted and M-Promoted Co/TiO$_2$ Catalysts (M = Zr, K, Cs): Effects of Crystal Phase of Supports and Metal−Support Interaction on Tuning Product Distribution

Wenhui Li,[†] Guanghui Zhang,[†] Xiao Jiang,[‡] Yi Liu,[†] Jie Zhu,[†] Fanshu Ding,[†] Zhongmin Liu,[§] Xinwen Guo,*[,†] and Chunshan Song*[,†,‖]

[†]State Key Laboratory of Fine Chemicals, PSU-DUT Joint Center for Energy Research, School of Chemical Engineering, Dalian University of Technology, Dalian 116024, People's Republic of China

[‡]School of Chemical and Biomolecular Engineering, Georgia Institute of Technology, Atlanta, Georgia 30332, United States

[§]National Engineering Laboratory for Methanol to Olefins, Dalian National Laboratory for Clean Energy, Dalian Institute of Chemical Physics, Chinese Academy of Sciences, Dalian 116023, People's Republic of China

[‖]Clean Fuels & Catalysis Program, EMS Energy Institute, PSU-DUT Joint Center for Energy Research, Departments of Energy and Mineral Engineering and Chemical Engineering, The Pennsylvania State University, University Park, Pennsylvania 16802, United States

S *Supporting Information*

ABSTRACT: Cobalt catalysts supported on TiO$_2$ with different crystal forms (anatase and rutile) differ sharply in CO$_2$ conversion and product selectivity for CO$_2$ hydrogenation. The Co/rutile-TiO$_2$ catalyst selectively catalyzed CO$_2$ hydrogenation to CH$_4$, while CO is the main product on the Co/anatase-TiO$_2$ catalyst. In situ DRIFT (diffuse reflectance infrared Fourier transform) results have partially revealed the reaction pathway of CO$_2$ hydrogenation on these two catalysts. On Co/rutile-TiO$_2$, the reaction proceeds through the key intermediate formate species, which is further converted to CH$_4$. Differently, the reaction on Co/anatase-TiO$_2$ undergoes CO$_2$ → *CO, which desorbs to form gas-phase CO instead of subsequent hydrogenation. The strongly bonded *CO is required to enhance the subsequent hydrogenation. By simply changing the calcination temperature of anatase TiO$_2$, the product selectivity can be tuned from CO to CH$_4$ with a significant increase in CO$_2$ conversion due to the surface phase transition of the anatase to the rutile phase. The addition of Zr, K, and Cs further improves the CO, CO$_2$, and H$_2$ adsorption in both the capacity and strength over anatase- and rutile-supported catalysts. The Zr modification makes the reaction pathway over anatase-supported catalyst proceed via the intermediate formate species and enables the subsequent hydrogenation to CH$_4$. In addition, the surface C/H ratio increases significantly in the presence of promoters (unpromoted < Zr-promoted < K-Zr-promoted ∼ Cs-Zr-promoted), which leads to the highest C$_2^+$ selectivity of 17% with 70% CO$_2$ conversion over K-Zr-Co/anatase-TiO$_2$ catalyst. These results reveal mechanistic insights into how the product distribution of Co/TiO$_2$ catalysts can be manipulated through adjusting the adsorption performance and surface C/H ratio.

KEYWORDS: CO$_2$ hydrogenation, cobalt catalyst, crystal phase, TiO$_2$, C/H ratio
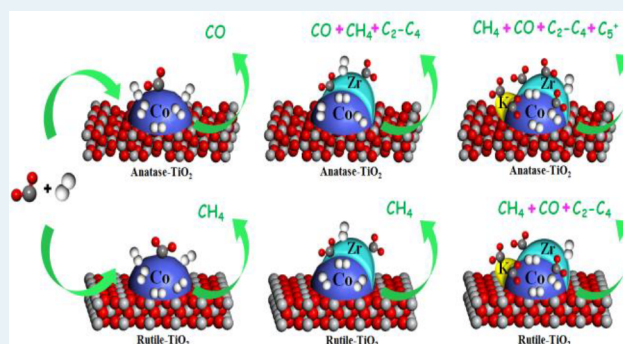
INTRODUCTION

Controlling the growth of CO$_2$ (carbon dioxide) concentration in the atmosphere is a major challenge facing the world today. Limiting CO$_2$ emission, CO$_2$ capture and storage, and CO$_2$ conversion and utilization are the primary ways to decrease the CO$_2$ concentration.[1,2] Carbon dioxide capture and storage (CCS) has the issue of potential leakage;[2,3] therefore, the chemical reduction of CO$_2$ over heterogeneous catalysts has aroused increasing interest recently as a complementary measure. Converting CO$_2$ into useful chemical is regarded as

a promising approach to not only mitigate CO$_2$ release, but also benefit the development of "carbon" industry.

Catalysts of CO$_2$ hydrogenation have been intensely investigated to improve the efficiency of CO$_2$ conversion. Supported metal catalysts are the classic materials for CO$_2$ conversion because of the special metal−support interaction. The similarity between CO and CO$_2$ hydrogenation

enlightened researchers to apply Fischer−Tropsch synthesis (FTS) catalysts for reference, such as Fe-,[4−8] Co-,[9−12] and Ni-based[13,14] catalysts. Fe- and Co-based catalysts both display excellent performance in FTS; however, Co-based catalysts selectively produce methane rather than the long-chain hydrocarbons when CO is replaced with CO_2 as the carbon source.[5] Lietti et al.[15] developed a deep understanding of the difference between CO and CO_2 hydrogenation on Co- and Fe-based catalysts. They elucidated that the CO and CO_2 adsorption strengths can affect the surface C/H ratio on catalysts. The key factor that manipulates the product distribution is the surface C/H ratio, which is tunable by the choices of catalysts.

In addition, the supports also play a vital role in the product distribution over an identical active metal. Chen et al.[16] recently found that PtCo bimetallic catalysts were capable of shifting the selectivity from CO to CH_4 by altering the oxide supports from TiO_2 to ZrO_2. In addition, metal oxide supports with the same chemical composition but different crystal phases also influence the catalytic performance. Kim et al.[17] synthesized a monodispersed 2 nm RuO_2 nanoparticle colloidal suspension and impregnated it onto TiO_2 with different crystal phases for CO_2 methanation. The activity and product selectivity were strongly dependent on the composition of the different crystal phases of TiO_2, wherein P25, with 20% anatase and the rest rutile, gave the highest CO_2 conversion and CH_4 selectivity. Lin et al.[18] also observed a similar phenomenon on Ni/TiO_2 catalysts with different TiO_2 crystal phases for both CO and CO_2 methanation. They proposed that rutile-TiO_2 significantly enhanced the CO dissociation and hydrogenation ability of Ni. Formate species, which are generally considered as the key intermediates of CO_2 methanation, were observed over Ni/rutile-TiO_2. However, the formate species were barely evidenced over Ni/anatase-TiO_2. The current results have demonstrated that anatase- and rutile-supported catalysts give different product selectivities for CO_2 hydrogenation. Actually, the different catalytic performances caused by the crystal phase possess different reaction pathways.

Zhang et al.[19] have improved the CO_2 turnover frequency of Ru/rutile-TiO_2 catalysts through pretreatment over CO_2 hydrogenation. They found that high-temperature pretreatment can increase the catalyst activity through changes in the thickness of TiO_x layers and the number of hydroxyl groups on the TiO_x surface. Song et al.[20,21] found that promoters, such as K and La, can adjust the product distribution on Fe-based catalysts over CO_2 hydrogenation. To date, Co-based supported catalysts applied for the CO_2 hydrogenation to C_2^+ hydrocarbons have rarely been reported in the literature. Can the product distribution be tuned on Co/TiO_2 through pretreatment and modification? With this in mind, this study prepared and characterized Co-based catalysts supported on anatase and rutile TiO_2 and evaluated their activity performance for CO_2 hydrogenation. The Co/rutile-TiO_2 catalyst selectively catalyzed CO_2 hydrogenation to CH_4, while CO is the main product on the Co/anatase-TiO_2 catalyst with relatively lower CO_2 conversion. It is worth noting that Co/anatase-TiO_2, calcined at 800 °C, exhibited significantly different catalytic performance in comparison to that calcined at 500 °C but displayed catalytic performance similar to that of Co/rutile-TiO_2 calcined at 500 °C, as well as having a similar reaction pathway. To clarify the origins for such interesting variation, these catalysts were characterized by XRD, H_2-TPR,

CO_2-TPD, CO-TPD, XPS, and in situ DRIFT. Inspired by the reaction pathway for the Co/TiO_2 catalysts, we prepared Zr-, K-, and Cs-promoted catalysts supported on different crystal phases of TiO_2 for CO_2 hydrogenation to give value-added C_2^+ hydrocarbons. The Zr, K, and Cs modification tuned the surface C/H ratio of catalysts effectively and led to higher C_2^+ hydrocarbon selectivity. This study reveals the essential influence of the supports on the Co-based catalysts for CO_2 hydrogenation from the perspective of Co chemical states, reactant adsorption, and reaction mechanism and offers an avenue to tune the surface C/H ratio of catalyst to manipulate the product distribution.

2. EXPERIMENTAL SECTION

2.1. Catalyst Preparation. Co/TiO_2 catalysts were prepared through impregnation using cobalt nitrate hexahydrate (Aladdin Chemicals) and TiO_2 with different crystal phases (anatase and rutile) (Aladdin Chemicals), giving a metal loading of 10 wt % Co. The anatase TiO_2 was calcined at 500, 600, 700, and 800 °C in a muffle furnace prior to catalyst preparation. The prepared catalysts were dried for 12 h at 120 °C and then calcined for 4 h at 500 °C. Co-Zr/TiO_2 catalysts were synthesized by the coimpregnation method using cobalt nitrate hexahydrate (Aladdin Chemicals) and zirconium oxynitrate dihydrate (Aladdin Chemicals) aqueous solutions with 10 wt % loading of both Co and Zr. The prepared catalysts were dried by similar procedures. The K- or Cs-promoted catalysts were also synthesized through the impregnation method using Co-Zr/TiO_2 catalysts as substrates with 10 wt % loading. The precursors of K and Cs are potassium nitrate (Aladdin Chemicals) and cesium nitrate (Aladdin Chemicals), respectively. The obtained catalysts are denoted as m-A(R)-x, where A represents the anatase support, R represents the rutile support, m stands for the metallic elements other than cobalt, and x represents the calcination temperature of anatase support.

2.2. Catalytic Test. The catalytic performance of catalysts was determined in a continuous-flow, high-pressure, fixed-bed reactor. Typically, 0.5 g of catalyst was placed in the reactor (inner diameter 8 mm). The catalyst was pretreated in hydrogen for 8 h at 400 °C before reaction. Then, the reactant gas mixture (3600 mL min^{-1}) with a H_2/CO_2 ratio of 4/1 and a pressure of 3 MPa was introduced into the reactor, followed by heating to 400 °C.

The effluents were quantitatively analyzed online with a FULI GC-97 gas chromatograph equipped with thermal conductivity and flame ionization detectors. Equations 1 and 2 were used to calculate the CO_2 conversion and the product selectivity:

$$CO_2 \text{ conversion } (\%) = \frac{n_{CO_2,in} - n_{CO_2,out}}{n_{CO_2,in}} \times 100\% \quad (1)$$

$$S_i \ (\%) = \frac{m_i n_{i,out}}{n_{CO_2,in} - n_{CO_2,out}} \times 100\% \quad (2)$$

where $n_{CO_2,in}$ and $n_{CO_2,out}$ represent moles of CO_2 at the inlet and outlet, respectively, $n_{i,out}$ represents molar of product i at the outlet, and m_i denotes the moles of C of the individual product at the outlet.

2.3. Characterization of Catalysts. The N_2 adsorption data such as surface area (BET) and pore size distribution (BJH) of the samples were obtained by using a Quantachrome
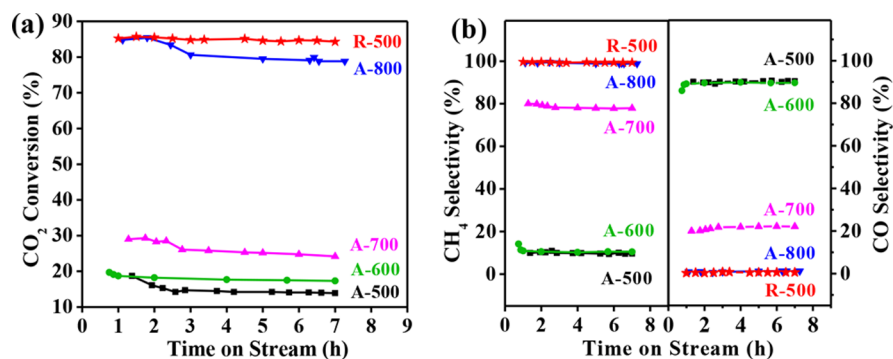
Figure 1. (a) CO_2 conversion and (b) product distribution over Co/TiO_2 catalysts. Conditions: H_2/CO_2 = 4/1, P = 3 MPa, GHSV = 7200 mL g^{-1} h^{-1}, T = 400 °C.

AUTO-SORB-1-MP sorption analyzer at 77 K. The catalysts were treated under vacuum at 300 °C for 2 h before the test.

A Tecnai F30 HRTEM instrument (FEI Corp.) operated at 300 kV was used to get the TEM images. The samples dispersed in ethanol were dropped on copper grids for TEM observation.

Temperature-programmed H_2 reduction (H_2-TPR) and desorption (H_2-TPD) were carried out on a ChemBETPulsar TPR/TPD apparatus (Quantachrome, USA). In the H_2-TPR program, the samples were heated from 25 to 900 °C at 10 °C min^{-1} with a total flow rate of 30 mL min^{-1} (5 vol % H_2/Ar). In the H_2-TPD program, samples were reduced for 2 h at 400 °C and flushed with Ar for 30 min. Then, the sample was cooled to 30 °C to adsorb hydrogen. After the samples were purged with argon gas for 30 min, the TPD program was performed in a range of 25−850 °C at a heating rate of 10 °C min^{-1}. CO-TPD and CO_2-TPD were performed on the same apparatus with a similar procedure.

X-ray photoelectron spectra (XPS) were conducted on a VG ESCALAB250 spectrometer. Prior to the measurements, the samples were passivated in 1% O_2/N_2.

X-ray diffraction (XRD) patterns were obtained by a RigakuSmartLab (9) diffractometer with Cu Kα radiation (λ = 1.5406 Å). The relative content of the crystal phase was calculated according to the diffraction peak intensity through MDI Jade 5.0 software.

In situ diffuse reflectance infrared Fourier transform (DRIFT) spectroscopy was conducted on an EQUINOX-55 Fourier transform infrared spectrometer (Bruker) equipped with a high-temperature reaction chamber and a mercury cadmium telluride (MCT) detector. Before the test, 30 mg of the sample was reduced in a hydrogen flow (40 mL/min) at 400 °C for 2 h. The background spectrum was collected subsequently when the temperature of the reaction chamber decreased to 50 °C. Then, the prereduced catalysts were exposed to H_2/CO_2 feed gas (H_2/CO_2 = 4) with 20 mL min^{-1} flow rate. The spectra were recorded in the temperature range from 50 to 400 °C.

3. RESULTS AND DISCUSSION

3.1. Effect of TiO_2 Crystal Phase on Catalytic Performance of Co/TiO_2.
Figure 1 shows the CO_2 conversion (Figure 1a) and product selectivity (Figure 1b) over Co/TiO_2 catalysts. In general, the activity of Co/r-TiO_2 catalyst is remarkably better than that of Co/a-TiO_2 catalysts under the same reaction conditions. On Co/r-TiO_2 calcined at 500 °C, the CO_2 conversion is 85.5% and the CH_4 selectivity is

99.8%. In striking contrast, the corresponding values over Co/a-TiO_2 catalyst, calcined at the same temperature, are much lower, namely 14.1% and 10.5%, respectively, and the main product is CO on the A-500. The product distribution under different CO_2 conversions over A-500 and R-500 are also shown in Table S1. The data shown in Table S1 illustrate the similar product distributions: that is, the R-500 catalyst selectively catalyzed CO_2 to CH_4, while CO is the main product on the A-500 catalyst. By an increase in the calcination temperature to 800 °C, a considerable rise in CH_4 selectivity and CO_2 conversion is observed over Co/a-TiO_2 catalysts. The CO_2 conversion of A-800 even reaches 80%. With an increase in calcination temperature, the gap in catalytic performance between Co/r-TiO_2 and Co/a-TiO_2 catalysts becomes narrow. Notably, the A-800 catalyst exhibits activity and selectivity comparable to those of R-500. Apparently, such calcination-temperature-dependent catalytic performance indicates the existence of key factors that is beneficial to CH_4 formation. To clarify that in conjunction with the difference in catalytic behavior among rutile- and anatase-supported catalysts, various characterization analyses were carried out, as discussed in the following section.

XRD patterns of the Co/TiO_2 samples in the calcined form are presented in Figure 2a. All Co/a-TiO_2 samples show a clear diffraction peak centered at 25.3°, which is typical for titania with the anatase phase (JCPDS 21-1272). The Co/r-TiO_2 sample shows a distinct diffraction peak centered at 27.5°, corresponding to titania with the rutile phase (JCPDS 21-1276). The intensity of the diffraction peak centered at 25.3° is enhanced with increasing calcination temperature on Co/a-
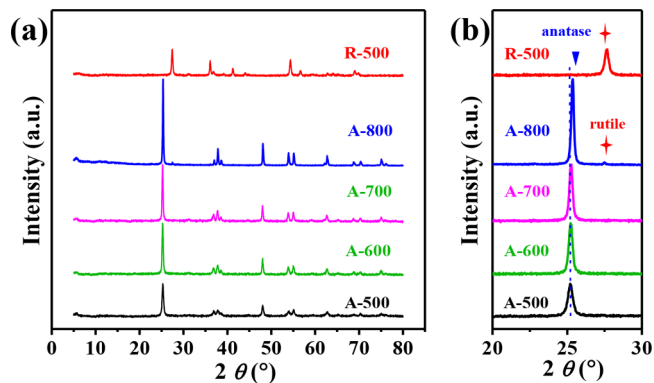

Figure 2. XRD patterns of (a) Co/TiO_2 catalysts in the region of 5−80° and (b) magnified region between 20 and 30°.

TiO_2 catalysts. Additionally, the diffraction peak centered at 27.5°, associated with rutile, emerges on A-800, and the content is less than 2%. Despite the fact that the anatase phase still dominates after 800 °C calcination, a phase transition from anatase to rutile occurs, which begins from the oxide surface.[22] As XRD is a means to detect the bulk crystal structure, the diffraction peak intensity of surface rutile contributes little to the A-800 sample. However, the supported cobalt species prefer to interact with the surface TiO_2, which is crucial in the catalytic reaction. As shown in Figure 2b, the diffraction peak centered at 25.3° of A-800 shifts to a higher degree by 0.2°. The generation of lattice distortion implies the tendency of a phase transition with an increase in calcination temperature. Evidently, XRD patterns confirm that the anatase phase still dominates even after the high-temperature calcination. However, the active surface phase has been transformed into a rutile phase. Therefore, the A-800 exhibits activity and selectivity comparable to those of R-500 due to the surface phase transition of anatase to rutile phase.

To clarify the nature of the titania physical properties, the N_2 adsorption data are offered in Table S1 and the pore size distribution is shown in Figure S1. The N_2 adsorption data show no micropores on both anatase and rutile titania, and the total pore volume is contributed by the intergranular space. In addition, the pore size distributions of the anatase and rutile samples are similar, and the specific surface area of rutile (35 m^2/g) is lower than that of the low temperature calcined anatase (59 m^2/g). The morphologies of reduced Co-TiO_2 catalysts were determined by high-resolution TEM. The TEM images in Figure 3a−c show that the size of Co nanoparticles
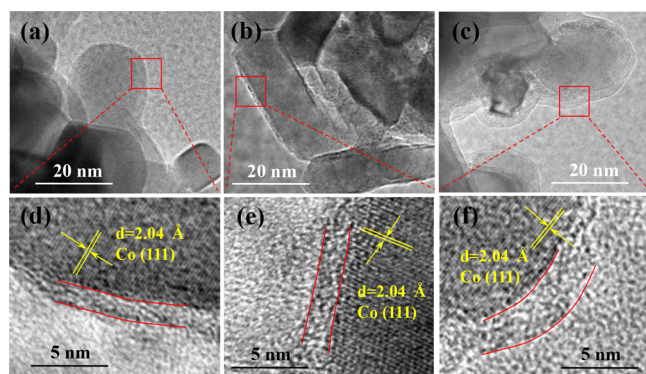

Figure 3. TEM images of reduced (a) A-500, (b) R-500, and (c) A-800 catalysts and their corresponding magnified TEM images in (d)−(f), respectively.

(NPs) supported on TiO_2 is about 20 nm, which can also be obtained from the Co particle size distribution (Figure S3), and the size of both anatase and rutile TiO_2 is ca. 40 nm. Figure 3d−f shows that Co NPs are covered by a thin TiO_2 overlayer, the thickness of which is about 2 nm after reduction. Furthermore, such a thin layer is evidenced for both A-500 and R-500. It is postulated that the TiO_x layer is derived from the TiO_2 support under the H_2 atmosphere during high-temperature pretreatment. A similar phenomenon was also reported previously, which was due to the migration of TiO_x in a high-temperature H_2 pretreatment.[23−26] Such an explanation shall also be valid in the present work. However, upon 800 °C calcination, the thickness of the overlayer increases to 3−4 nm, indicating a stronger metal−support interaction in the high-temperature calcined anatase TiO_2. Such a stronger metal−

support interaction likely results in lattice distortion, as evidenced by the peak shift in the corresponding XRD pattern (Figure 2). Levin et al.[27] have investigated the correlation of titania overlayers with the catalytic performance of Rh/TiO_2 in CO hydrogenation and stated that the methanation rate goes through a maximum with increasing TiO_x coverage. Herein, the increased thickness of titania overlayers on A-800, in comparison to that on A-500, appears to correlate to the enhancement of CO_2 methanation (Figure 1), demonstrating the key role of a strong metal−support interaction in governing the activity performance on TiO_2-supported Co catalysts.

Figure 4 depicts the TPR profiles for Co_3O_4/TiO_2 calcined catalyst precursors to reveal the reducibility of Co/TiO_2
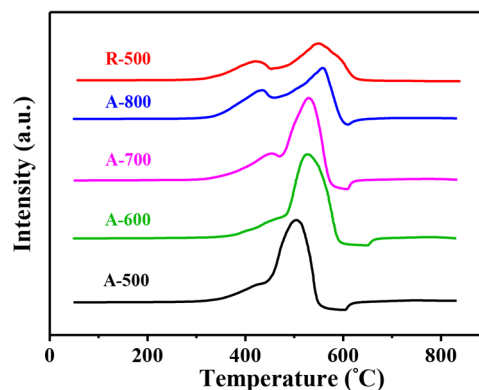

Figure 4. H_2-TPR profiles of Co/TiO_2 catalysts.

catalysts and the interaction between Co_3O_4 and the TiO_2 support. All Co_3O_4/TiO_2 catalysts exhibit two reduction peaks centered at 310−480 and 450−620 °C. The former corresponds to the reduction of Co_3O_4 to CoO, while the latter can be assigned to the reduction of CoO to Co.[28] In addition, the second peak of the R-500 catalyst shifts to higher temperatures (e.g., from 500 to 550 °C) in comparison with that of A-500, suggesting an intensified Co−TiO_2 interaction.[29] When the anatase TiO_2-supported catalysts are calcined at high temperatures, namely ranging from 500 to 800 °C, the reduction temperature of Co_3O_4 gradually shifts to higher temperatures, which are close to those of R-500 samples. The reduction extent of catalysts is shown in Table S3. Hence, the higher reduction temperature of Co_3O_4 elucidates the strengthened metal−support interaction on R-500 and A-800.

CO_2-TPD profiles in Figure 5a can be divided into three regions,[30,31] 50−150, 150−250, and >250 °C, corresponding to weak, medium, and strong adsorption, respectively.[32] On the A-500 sample, only a weakly bonded species is evidenced. With an increase in calcination temperature, a distinct shift of adsorption behavior from weakly bonded species to moderately bonded and ultimately to strongly bonded species is observed over anatase-supported catalysts.

TPR results already demonstrate the temperature-dependent metal−support interaction between Co and TiO_2, in which the interaction grows stronger with an increase in calcination temperature, especially for A-800 and R-500. Clearly, such a strengthened interaction accounts for the characteristic adsorption behavior toward moderately and strongly bonded species on the same catalysts. More interestingly, not only do A-800 and R-500 have analogous CO_2 adsorption behavior but they also exhibit comparable and superior CO_2 conversion
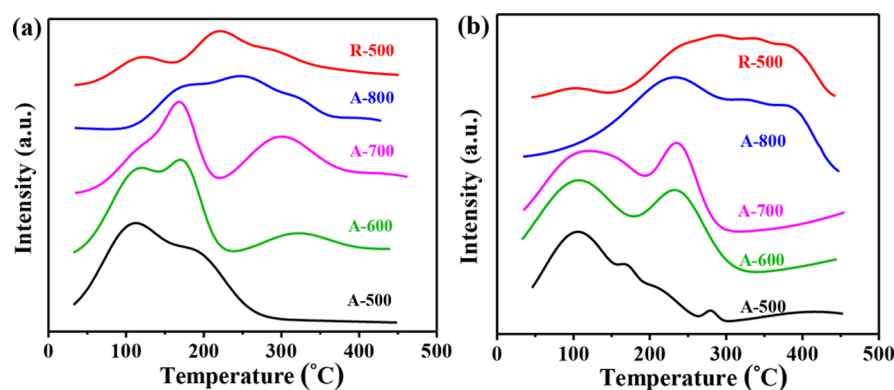
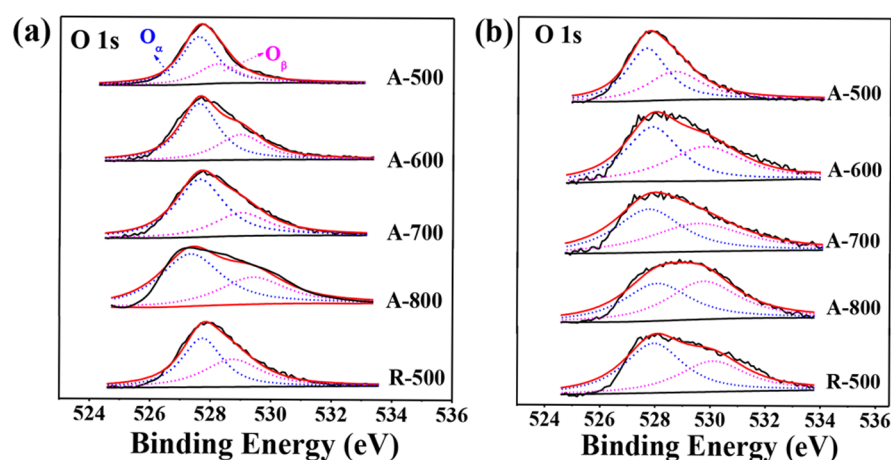**Figure 5.** CO_2-TPD (a) and CO-TPD (b) profiles of Co/TiO_2 catalysts.

Figure 6. XPS spectra of O 1s on (a) calcined Co/TiO_2 catalyst precursors and (b) reduced and passivated Co/TiO_2 catalysts.

(Figure 1). As reported, in comparison with H_2 dissociation and H* migration, CO_2 activation is more difficult and crucial in the CO_2 hydrogenation process.[33,34] The best CO_2 adsorption capacity of A-800 and R-500 catalysts might facilitate the CO_2 conversion.

An ideal catalyst should not only adsorb the reactant with the proper strength in the initiation but also bond the intermediates strongly enough in propagation and weakly enough in desorption. As one of the reaction pathways, CO is a pivotal intermediate in CO_2 conversion.[35,36] Therefore, CO adsorption properties were evaluated by CO-TPD for Co/TiO_2 catalysts, as presented in Figure 5b. A-500 only displays adsorption at low temperatures (i.e., <150 °C), corresponding to weakly bonded species. The desorption temperature shifts to higher temperature with an increase in calcination temperature, indicating stronger CO adsorption. In addition, A-800 has CO adsorption behavior analogous to that of R-500. Interestingly, such a temperature-derived adsorption shift appears to resemble the CO_2 adsorption on the same catalysts.

CO selectivity mainly depends on the bonding ability of the metal−oxide interface with CO.[16,37−39] Due to the facile desorption of *CO, the metal−oxide interface should be selective to CO. In contrast, when the bond between the metal−oxide interface and *CO is strong, the *CO is inclined to hydrogenation or dissociation than desorption, thereby leading to lower CO selectivity and higher selectivity to the desired CH_4. Considering the catalytic performance in Figure 1b, A-500 selectively produces CO and the CO selectivity decreased with an increase in calcination temperature. In

association with the CO adsorption properties, weak CO adsorption gives high CO product selectivity, and strong CO adsorption offers a high possibility for a subsequent hydrogenation to CH_4. Therefore, it is suggested that the adsorbed CO favors desorption rather than the subsequent hydrogenation on A-500, thereby leading to a selective production of CO. In contrast, the strongly adsorbed CO on A-800 and R-500 is highly conducive to the subsequent hydrogenation, resulting in higher selectivity to the targeted CH_4.

Figure 6a presents the O 1s XPS spectra for calcined catalyst precursors and Figure 6b those for reduced and passivated catalysts. The intense peak at 527.8 eV can be associated with the lattice oxygen (O_α) in TiO_2, while the peak at 529.5 eV can be attributed to the surface hydroxyl groups or the adsorbed oxygen (O_β).[40,41] The O_β to O_T ($O_T = O_\alpha + O_\beta$) ratio was calculated and is gathered in Table 1 on the basis of the area integrals. Deconvolution analysis indicates that the peak of surface hydroxyl groups/adsorbed oxygen gradually shifts to

Table 1. XPS Data for As-Prepared Catalysts

sample	O_β/O_T (%)	
	fresh calcined	H_2 reduced and passivated
A-500	37.1	46.7
A-600	31.1	41.8
A-700	31.3	47.5
A-800	35.1	51.5
R-500	35.3	49.8

higher binding energy from A-500 to A-800. Moreover, the same peak of R-500 also exhibits a binding energy higher than that of A-500. These observations indicate the electron deficiency on rutile TiO_2 and anatase TiO_2 after high-temperature calcination. In Figure 6b, the peak of surface hydroxyl groups/adsorbed oxygen becomes stronger in comparison to that for the corresponding calcined catalysts. As given in Table 1, all reduced catalysts present higher O_β/O_T ratios in comparison to the corresponding calcined catalysts, among which the ratios of A-800 and R-500 are approximately 1.5 times as much as those for the corresponding calcined catalyst precursors. Notably, the reduced A-800 exhibits a higher ratio of O_β/O_T in comparison to A-500, indicating a reduction of lattice oxygen O_α on A-800. The surface reconstruction may occur in the reduced titania to avoid producing any five-coordinate titania.[42] However, the reconstructed titania possesses lower lattice oxygen content in comparison with the unreduced titania. In other words, such behavior implies an increase in anion vacancies and defects upon reduction. The defects on the A-800 and R-500 catalysts are expected to adsorb and activate CO_2 and CO.[43] As is known in the literature, the peaks at high temperatures in CO_2- and CO-TPD profiles originate from desorption of CO_2 and CO that interact strongly with anion vacancies.[44] Hence, the lower the oxygen content, the more strongly adsorbed CO_2 and CO are, which is beneficial to the CO_2 activation and the subsequent hydrogenation to CH_4. In addition, there are more reduced cobalt species on the reduced and passivated A-800 and R-500 obtained from the Co 2p XPS data (Figure S2 and Table S3).

To identify the adsorbed reaction intermediates and the gas-phase composition in CO_2 hydrogenation, DRIFTS measurements were performed on A-500, R-500, and A-800. The in situ reduced catalysts were exposed to the feed gas, and the DRIFT spectra were recorded at temperatures ranging from 50 to 400 °C with 50 °C as an interval, as shown in Figure 7. The employment of the reactive mixture at 50 °C results in the appearance of an adsorption band at 1222 cm^{-1} on both anatase- and rutile-supported catalysts, corresponding to the $\delta(OH)$ bending of bicarbonate (HCO_3*) originating from the CO_2 adsorption.[45,46] The broad band located at 3100−3500 cm^{-1} is associated with the hydroxyl.[19,47] The band centered at 1418 cm^{-1} between 50 and 100 °C is related to the O−C−O vibration of bicarbonate on both R-500 and A-800.[48,49] As displayed in Figure 7b,c, at >100 °C, the bicarbonates are hydrogenated to formate species, featured by characteristic bands at 1360 and 1570 cm^{-1} associated with the O−C−O stretching of formate.[50−52] This suggests that the reaction between CO_2 and H_2 can occur at relatively low temperatures. Along with the appearance of formate species, the chemisorbed CO centered at 1970 cm^{-1} is observed over R-500 catalyst[53] (Figure 7b); however, the gas-phase CO centered at 2100 cm^{-1} is evidenced over A-500 catalyst despite its weak intensity (Figure 7a).[28,54] On A-800, both the chemisorbed and gas-phase CO are detected (Figure 7c). The DRTFT results are in line with the CO-TPD data that the A-500 exhibits weak adsorption toward CO, while R-500 and A-800 possess stronger affinity with CO adsorption. Notably, bicarbonate and formate species and gas-phase CO are the only species identified in DRIFT spectra over A-500 catalyst (Figure 7a); CO is the preferential product of this catalyst. Clearly, the DRIFTS results are in accordance with the catalytic performance (Figure 1). The maximum intensity of formate species is
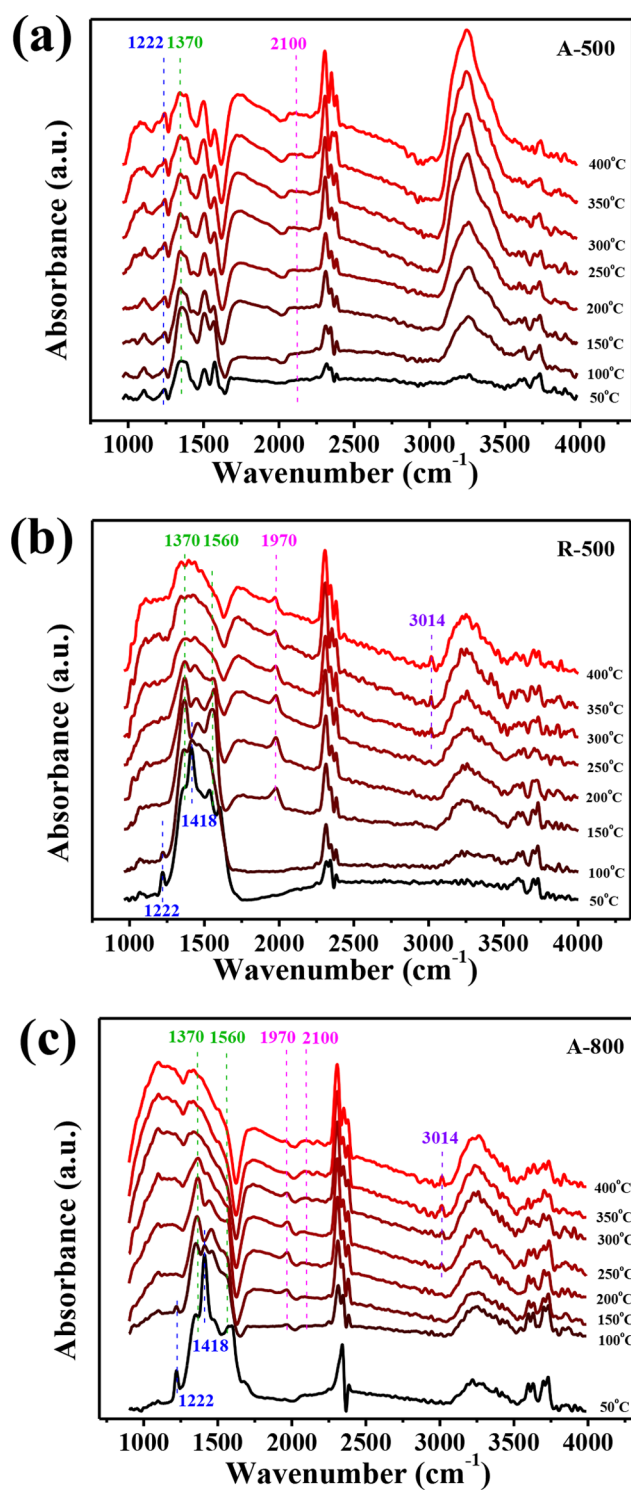

Figure 7. In situ DRIFT spectra of (a) A-500, (b) R-500, and (c) A-800.

observed at 250 °C. At the same temperature, the band centered at ca. 3014 cm^{-1}, assigned to the $\nu(CH)$ vibration mode of CH_4,[55,56] appears over R-500 and A-800, the intensity of which increases along with the decrease in formate species and chemisorbed CO, indicating that the further hydrogenation of CO to CH_4 has occurred. Chen et al.[16] recently found that PtCo bimetallic catalysts were capable of shifting the selectivity from CO to CH_4 by alteration of the oxide supports from anatase TiO_2 to ZrO_2. Experimentally, both
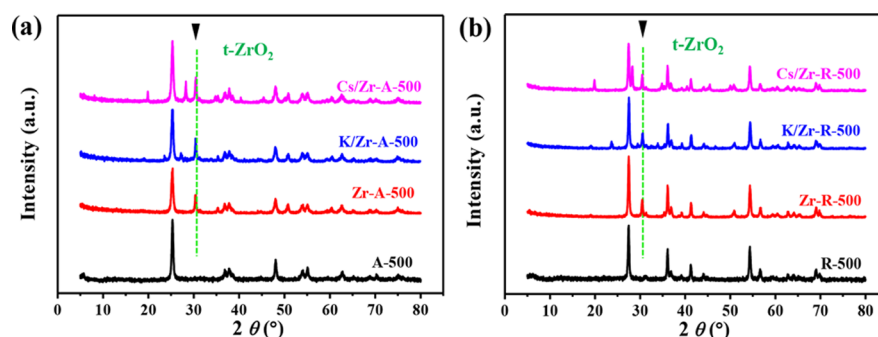
Figure 8. XRD patterns of (a) anatase-supported catalysts and (b) rutile-supported catalysts in the region of 5−80°.
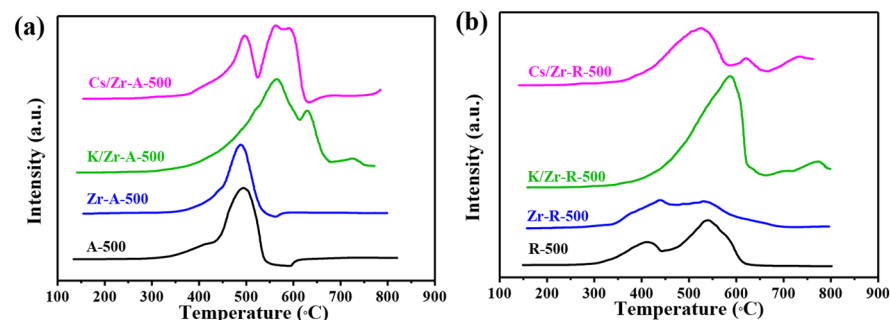

Figure 9. H$_2$-TPR profiles of (a) anatase- and (b) rutile-supported catalysts.

*HCOO and *HOCO were identified as reaction intermediates on both PtCo/TiO$_2$ and PtCo/ZrO$_2$, whereas *CH$_3$O was only evidenced on PtCo/ZrO$_2$. DFT results demonstrate that the CO desorption energy is much lower than that of its hydrogenation to *CHO on PtCo/anatase-TiO$_2$. Such an explanation shall also be valid in the present work. In situ DRIFT results have partially revealed the reaction pathway of CO$_2$ hydrogenation on these two catalysts: (i) formate is the key intermediate on the Co/rutile-TiO$_2$ catalyst and can be converted to CH$_4$; (ii) CO$_2$ can be transferred to CO on the Co/anatase-TiO$_2$ catalyst, and CO desorbs to the gas phase rather than proceeding through a subsequent hydrogenation.

3.2. Improving Catalytic Performance by Tuning the Surface C/H Ratio through Zr, K, and Cs Addition. On the basis of the above analysis and discussion, the adsorption of reactants and intermediates plays a pivotal role in determining the product distribution. Through a simple calcination, the anatase-supported catalysts are more active and prefer to generate CH$_4$ because of the intensified CO$_2$ and CO adsorption, as well as metal−support interactions. In our previous work, ZrO$_2$ was investigated to prepare Co-based catalysts and compared with various supports.[57] The Co/ZrO$_2$ catalyst gave enhanced CO$_2$ and CO adsorption in comparison with Co/Al$_2$O$_3$ catalyst. Bell et al. also found that the addition of Zr in the catalysts could increase the CO adsorption and the C$_5^+$ selectivity while suppressing the CH$_4$ selectivity under common reaction conditions for FTS.[58] Apart from this, the addition of K and other alkali metals enabled the tuning of the surface basicity, through which more adsorption sites are created for CO$_2$ adsorption on the surface.[7,20] In other words, the alkali-metal promoters were capable of shifting the selectivity from methane to the desired higher hydrocarbons by tuning the surface C/H ratios.[20,59] Inspired by those results, we continued the work by introducing Zr, K, and Cs to modifying the Co-based catalysts in an attempt to shift the

product distribution from CO to CH$_4$ and further to C$_{2+}$ hydrocarbons by manipulating the surface C/H ratios.

The Zr-, Zr-K-, and Zr-Cs-promoted catalysts were synthesized by a impregnation method using 500 °C calcined anatase and rutile TiO$_2$ as supports. The XRD patterns of prepared samples are shown in Figure 8. In comparison with the A-500 and R-500, the new diffraction peak of modified catalysts centered at 30° is associated with the tetragonal-ZrO$_2$.[60] The diffraction peaks of K$_2$O (23.6 and 27.4°, JCPDS 65-2992) and Cs$_2$O (28.2°, JCPDS 43-1005) are also presented after calcination on the K- and Cs-promoted catalysts. Clearly, the crystallinity of the support is well retained for both the anatase- and rutile-supported catalysts after the addition of Zr, K, and Cs.

Figure 9 depicts the TPR profiles for calcined catalyst precursors. The Zr addition barely changed the reduction properties of the catalysts; however, the addition of K and Cs has a great influence on the reduction behaviors of catalysts. On K/Zr-A-500 and Cs/Zr-A-500, the reduction peaks are split into three distinct peaks centered at 400−600, 500−650, and 550−800 °C. The first and second peaks can be assigned to the reduction of Co$_3$O$_4$ to CoO and CoO to Co, respectively. The third peak corresponds to the reduction of Co$_3$O$_4$, which has a stronger interaction with the TiO$_2$ support. For K/Zr-R-500 and Cs/Zr-R-500, the reduction peaks also obviously shift to higher temperature in comparison with R-500. The retarded reduction temperatures of K- and Cs-promoted catalysts suggest an intensified Co−TiO$_2$ interaction. Notably, the K-promoted catalysts, including both anatase- and rutile-supported catalysts, present the highest reduction temperature and maximum peak area of hydrogen consumption.

As discussed in the previous section, the adsorbed CO favors desorption rather than subsequent hydrogenation on A-500, thereby leading to a selective production of CO. In contrast,
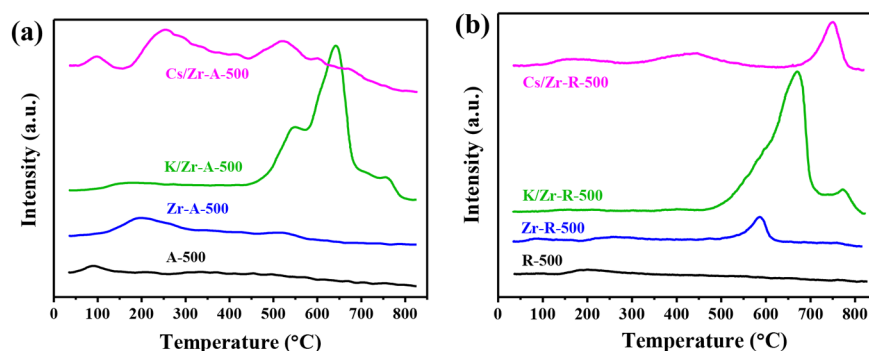
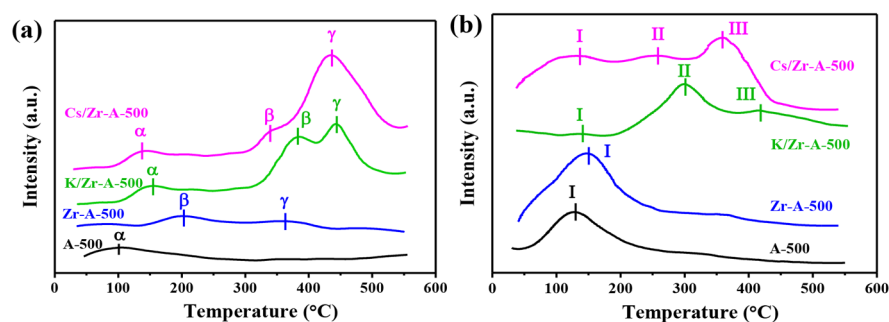**Figure 10.** CO-TPD profiles of (a) anatase- and (b) rutile-supported catalysts.

Figure 11. (a) CO_2-TPD and (b) H_2-TPD profiles of anatase-supported catalysts.

Table 2. CO_2 and H_2 Adsorption of Anatase-Supported Catalysts

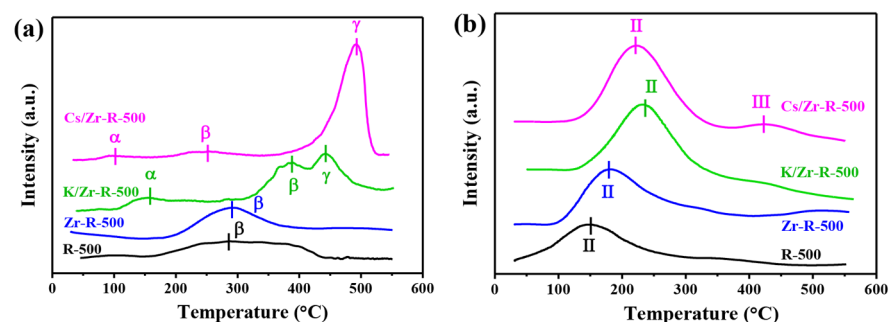| cat.	CO_2-TPD				H_2-TPD				C/H
	T_α (°C)	T_β (°C)	T_γ (°C)	CO_2 uptake (μmol $g_{cat.}^{-1}$)	T_I (°C)	T_{II} (°C)	T_{III} (°C)	H_2 uptake (μmol $g_{cat.}^{-1}$)	
A-500	101			109	130			205	0.26
Zr-A-500		202	363	210	147			291	0.36
K/Zr-A-500	150	382	444	631	135	302	415	328	0.96
Cs/Zr-A-500	136	338	434	847	134	253	360	412	1.02

Figure 12. (a) CO_2-TPD and (b) H_2-TPD profiles of rutile-supported catalysts.

the strongly adsorbed CO on A-800 and R-500 is highly conducive to the subsequent hydrogenation, resulting in a higher selectivity to the targeted CH_4. Apparently, tuning the CO adsorption capacity is crucial for an efficient CO_2 conversion. CO-TPD was also conducted on the modified catalysts, and the resulting profiles are shown in Figure 10. On Zr-A-500, the CO desorption temperature shifts from about 100 to 200 °C in comparison with A-500, corresponding to a moderate CO adsorption (Figure 10a). However, the Zr-R-500 exhibits a strong CO adsorption with the desorption peak centered at 550−600 °C (Figure 10b). When K and Cs are added to the Zr-modified catalysts, the CO desorption peaks

shift to higher temperatures but with distinct variations. In particular, the K-promoted catalysts possess the maximum strong CO adsorption at high temperature. To sum up, the addition of Zr, K, and Cs strengthens the CO adsorption markedly, which might benefit the subsequent hydrogenation.

The CO_2 and H_2 adsorptions were also determined on the modified catalysts. In Figure 11a, different adsorbed species are evidenced on the anatase-supported catalysts and are dependent on the addition of promoters. From low to high temperatures, these species are denoted as peaks α, β, and γ, respectively, and the positions of peaks α, β, and γ are given in Table 2. A-500 exhibits only weak adsorption of CO_2. When Zr

Table 3. CO$_2$ and H$_2$ Adsorption of Rutile-Supported Catalysts

	CO$_2$-TPD				H$_2$-TPD				
cat.	T_α (°C)	T_β (°C)	T_γ (°C)	CO$_2$ uptake (μmol g$_{cat.}^{-1}$)	T_I (°C)	T_{II} (°C)	T_{III} (°C)	H$_2$ uptake (μmol g$_{cat.}^{-1}$)	C/H
R-500		290		153	151			275	0.27
Zr-R-500		294		298	178			421	0.35
K/Zr-R-500	153	387	442	791	232			452	0.87
Cs/Zr-R-500	101	246	493	828	220	426		492	0.84

is added, the CO$_2$ desorption peaks shift to higher temperatures, corresponding to medium and strong CO$_2$ adsorption. On K- and Cs-promoted Zr-A-500, there is a large amount of strong CO$_2$ adsorption while there is almost no weak CO$_2$ adsorption. In particular, the K-added catalyst possesses the highest CO$_2$ desorption temperature. The addition of Zr, K, and Cs significantly improved the CO$_2$ adsorption in both capacity and strength. As depicted in Figure 11b, the H$_2$ adsorption behavior is also tunable by the addition of promoters, and three species are identified and denoted as I−III from low to high temperatures (Table 2). Similar to the case for CO$_2$ adsorption, A-500 exhibits only weak adsorption toward H$_2$. The addition of Zr barely changes the H$_2$ adsorption strength but notably improves the H$_2$ adsorption capacity. When K is added to Zr/A-500, the weak H$_2$ adsorption is dramatically suppressed, and medium and strong H$_2$ adsorptions emerge instead. On Cs/Zr-A-500, all adsorbed species are evidenced and greatly improved, especially for the strongly bonded species. On the basis of the area integrals of CO$_2$ and H$_2$ desorption peaks in Figure 11, the uptakes of adsorbed CO$_2$ and H$_2$ and the corresponding surface C/H ratios were calculated and are gathered in Table 2. In the presence of Zr, K, and Cs, the surface C/H ratios of promoted A-500 catalysts increase significantly. In comparison to A-500, the C/H ratios of K/Zr- and Cs/Zr-A-500 increased 2.7 and 3 times, respectively.

As shown in Figure 12 and Table 3, the Zr-, K-, and Cs-promoted rutile-supported catalysts generally display adsorption behaviors similar to those of the anatase-supported catalysts in terms of the CO$_2$ and H$_2$ adsorption: the addition of Zr, K, and Cs significantly improves the CO$_2$ and H$_2$ adsorption in both the capacity and strength. However, unlike the anatase-supported catalysts, the modified rutile-supported catalysts mainly exhibit the medium H$_2$ adsorption instead of the strong H$_2$ adsorption on the anatase-supported catalysts. The surface C/H ratio also increases with the addition of promoters. Therefore, the addition of Zr, K, and Cs effectively improves the capacity and strength of CO$_2$ adsorption and suppresses the weak H$_2$ adsorption.

The modified catalysts were applied to the CO$_2$ hydrogenation, and the catalytic performance is shown in Figure 13. As mentioned previously, the A-500 mainly produces CO while R-500 selectively yields CH$_4$. When Zr is added to the catalysts, the CO selectivity is decreased to 50%, while the production of C$_2$−C$_4$ alkane takes place over Zr-A-500 (Figure 13a). It is speculated that the enhanced hydrocarbon production originates from the stronger CO adsorption capability of Zr-A-500 (Figure 10a). When K and Cs are added to Zr-A-500, CO selectivity is drastically decreased to less than 10%. Although CH$_4$ becomes the main product, C$_2^+$ product selectivity is improved significantly and reaches the maximum C$_2^+$ product selectivity at 17%. This could be associated with the intensified CO$_2$ and H$_2$ adsorption over K/Zr-A-500 and Cs/Zr-A-500. Cs/Zr-A-500 shows the highest
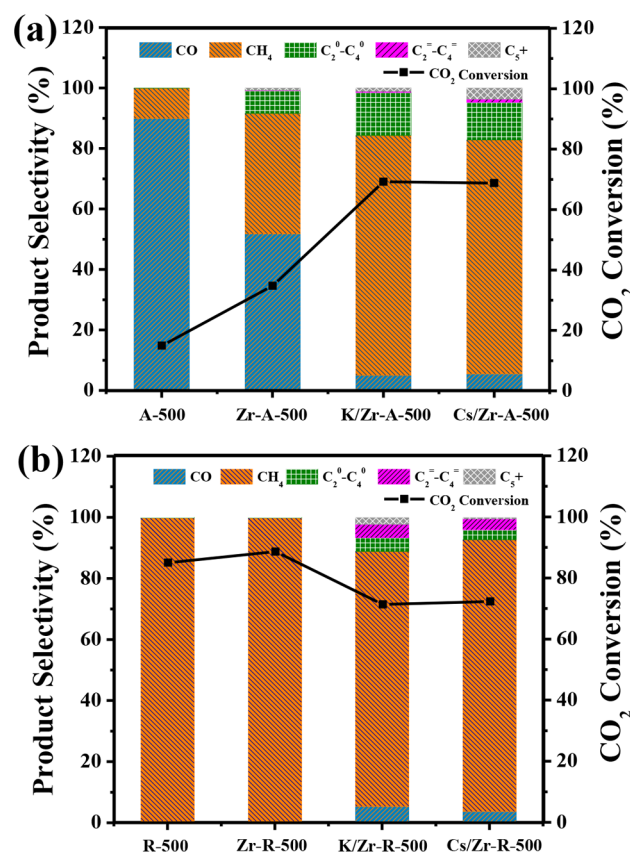

Figure 13. Catalytic performance of (a) anatase- and (b) rutile-supported catalysts. Conditions: H$_2$/CO$_2$ = 4/1, P = 3 MPa, GHSV = 7200 mL g^{-1} h^{-1}, T = 400 °C.

C$_5^+$ selectivity, which can be related to the greatly improved adsorption toward strongly bonded CO$_2$ species and to the maximized surface C/H ratio. Additionally, the CO$_2$ conversion is also increased from 15% to 35% with the addition of Zr and further to 70% in the presence of K or Cs. Apperently, the surface C/H ratio increase is in favor of long-chain product generation rather than methane.

In spite of the improved CO, CO$_2$, and H$_2$ adsorption capacity over rutile-supported catalysts, the CO$_2$ conversion and product distribution of rutile-supported catalysts resemble those of the reference catalyst R-500 in general, even with a slight decrease of CO$_2$ conversion over K/Zr-R-500 and Cs/Zr-R-500. On both R-500 and Zr-R-500, the CH$_4$ selectivity is more than 99%, while K/Zr-R-500 exhibits the highest C$_2^+$ selectivity in comparison with other rutile-supported catalysts, which approaches 10%.

In situ DRIFTS measurements were performed on Zr-A-500 and Zr-R-500 to understand the reaction pathway for the Zr-modified catalysts. The in situ DRIFT spectra are shown in Figure 14. Similar to the R-500 catalyst, on the Zr-R-500
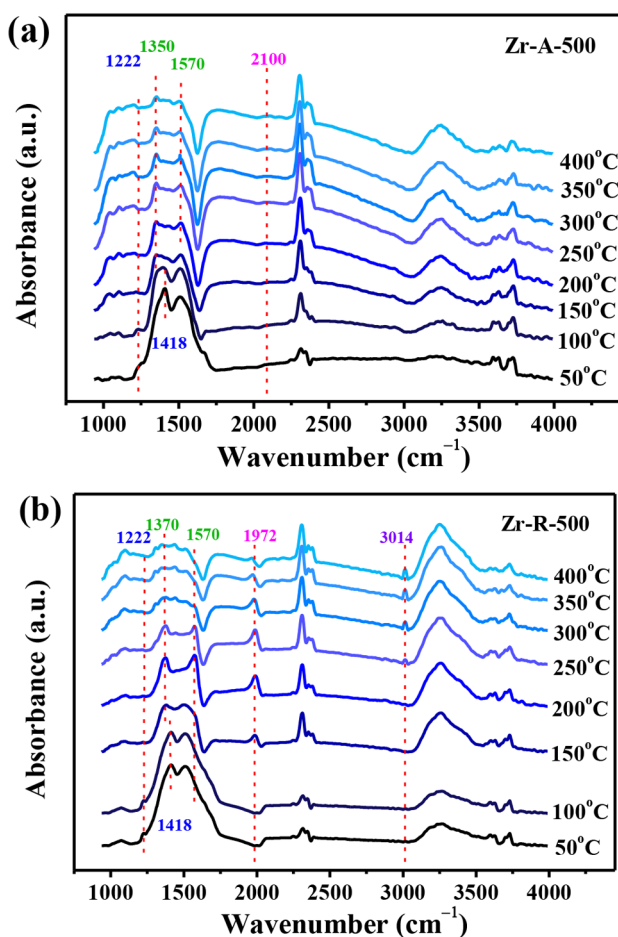
Figure 15. Plot of C_2^+ selectivity as a function of C/H ratio.

Figure 14. In situ DRIFT spectra of (a) Zr-A-500 and (b) Zr-R-500.

catalyst, the intensity of formate species (1350 and 1570 cm^{-1}) achieved a maximum and CH$_4$ (3014 cm^{-1}) appeared along with a decrease in formate species and chemisorbed CO (2100 cm^{-1}). On the basis of the previous analysis, on the A-500 catalyst, the formate species are the spectators and do not decrease during the reaction period. However, on the Zr-A-500 catalyst, the formate species (1350 and 1570 cm^{-1}) appeared at 200 °C and the intensity decreased at 350 °C. At the same time, on the Zr-A-500 catalyst, there is more CH$_4$ in the products. The result indicates that the Zr modification makes the reaction pathway over the anatase-supported change to a formate species intermediate pathway and enables the subsequent hydrogenation to CH$_4$.

To clarify the effect of C/H ratios on the product distribution, the C_2^+ selectivity is plotted as a function of C/H ratios in Figure 15. At low C/H ratios (i.e., C/H < 0.5), the C_2^+ selectivity of the rutile-supported catalysts increases slowly as the C/H ratio increases; in striking contrast, the C_2^+ selectivity increases quickly as the C/H ratio increases to C/H > 0.5. Interestingly, the trend of the anatase-supported catalysts is inverse. The C_2^+ selectivity increases obviously as the C/H ratio increases at a low C/H ratio (i.e., C/H < 0.5) over the anatase-supported catalysts. When the C/H ratio reaches a relatively high value, the C_2^+ selectivity increases slowly. Notably, the C_2^+ selectivity of the anatase-supported catalysts is always higher than that of rutile-supported catalysts. Even at the same C/H ratio, the C_2^+ selectivity differs, which is
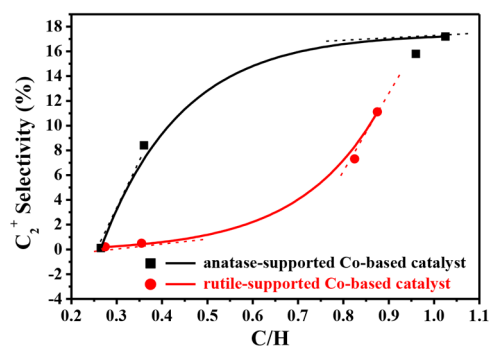
caused by the special metal−support interaction. In comparison with anatase-supported catalysts, there is less type III H$_2$ adsorption on rutile-supported catalysts after modification, which corresponds to the strongly bonded H$_2$ species. In addition, the type γ CO$_2$ desorption temperature on rutile-supported catalysts is higher than that on anatase-supported catalysts. The overly strong CO$_2$ adsorption is less active and leads to a decrease in CO$_2$ conversion. As a result, the appropriate adsorption strength of CO$_2$ and H$_2$ is beneficial to CO$_2$ conversion, and a higher C/H ratio results in higher C_2^+ selectivity.

4. CONCLUSION

Co-based catalysts supported on anatase, rutile, and high-temperature pretreated anatase TiO$_2$ were prepared by an impregnation method and evaluated for CO$_2$ hydrogenation. Co/r-TiO$_2$ catalyst selectively catalyzed CO$_2$ hydrogenation to CH$_4$ with 85% CO$_2$ conversion, while CO is the main product on Co/a-TiO$_2$ catalyst with relatively lower CO$_2$ conversion. By a simple change in the calcination temperature of anatase TiO$_2$, the product distribution can be tuned. When the calcination temperature increased to 800 °C, the Co/anatase-TiO$_2$ catalyst exhibited behavior similar to that of Co/rutile-TiO$_2$ catalyst, in which high CO$_2$ conversion (e.g., 85%) and CH$_4$ selectivity (e.g., 99%) are achieved. Therefore, the rutile phase supported cobalt catalyst is more active in CO$_2$ methanation and the A-800 exhibits activity and selectivity comparable to those of R-500 due to the surface phase transition of anatase to rutile phase.

Further surface analysis (XPS) reveals that anion vacancies and defects on these two series of catalysts are expected to adsorb and activate CO$_2$ and CO. The intensified CO adsorption on rutile-supported catalyst and calcined anatase-supported catalysts offer viability of the subsequent hydrogenation and preferential CH$_4$ formation. In contrast, the CO desorbs easily on anatase-supported catalyst, thereby leading to a selective production of CO rather than hydrogenation. In situ DRIFT results partially substantiate the reaction pathway of CO$_2$ hydrogenation on these two catalysts. The formate species is identified and suggested to be the key intermediate for CH$_4$ formation on Co/r-TiO$_2$ catalyst; however, it just transfers from CO$_2$ to CO without subsequent hydrogenation on Co/a-TiO$_2$ catalyst. The significant variation between the two different scenarios is that the generation of CH$_4$ requires a catalyst that bonds *CO strongly enough to enable the subsequent hydrogenation rather than desorption. These results give mechanistic insights into why the catalytic

performances of Co-based catalysts supported on anatase and rutile TiO_2 are different.

In order to generate more value-added products, Zr, K, and Cs were added to the anatase- and rutile-supported catalysts through an impregnation method to tune the product selectivity. After modification, the CO, CO_2, and H_2 adsorptions are improved in both the capacity and strength over modified anatase- and rutile-supported catalysts. It is surprising that CO_2 conversion over anatase-supported catalysts is improved markedly after adding Zr and K in the meantime. Zr modification makes the reaction pathway over the anatase-supported catalyst proceed via key intermediate formate species and enables the subsequent hydrogenation to CH_4. In particular, the surface C/H ratio increases significantly and follows the order unpromoted < Zr-promoted < K-Zr-promoted $\approx$ Cs-Zr-promoted. This leads to the highest C_2^+ selectivity of 17% with 70% CO_2 conversion over K/Zr-A-500. However, at a low C/H ratio (C/H < 0.5), on the modified rutile-supported catalysts, the C_2^+ selectivity increases slightly as the C/H ratio increases even with a slight decrease of CO_2 conversion. Evidently, an appropriate adsorption strength of CO_2 and H_2 is beneficial to CO_2 conversion, and a higher C/H ratio results in higher C_2^+ selectivity. As a result, the product distribution can be controllably regulated by adjusting the metal−support interaction and surface C/H ratio through Zr, K, and Cs modification over Co-based catalysts for CO_2 hydrogenation.

ASSOCIATED CONTENT

Ⓢ Supporting Information

The Supporting Information is available free of charge on the ACS Publications website at DOI: 10.1021/acscatal.8b04720.

> Catalytic performance, physical properties, pore size distribution, extent of reduction and adsorption data, and XPS and TEM data (PDF)

AUTHOR INFORMATION

Corresponding Authors
*E-mail for X.G.: guoxw@dlut.edu.cn.
*E-mail for C.S.: csong@psu.edu.

ORCID ⊙
Guanghui Zhang: 0000-0002-5854-6909
Xiao Jiang: 0000-0002-4902-1828
Xinwen Guo: 0000-0002-6597-4979
Chunshan Song: 0000-0003-2344-9911

Notes
The authors declare no competing financial interest.

ACKNOWLEDGMENTS

REFERENCES

(1) Sakakura, T.; Choi, J.; Hiroyuki, Y. Transformation of Carbon Dioxide. *Chem. Rev.* **2007**, *107*, 2365−2387.

(2) Dimitriou, I.; García-Gutiérrez, P.; Elder, R. H.; Cuéllar-Franca, R. M.; Azapagic, A.; Allen, R. W. K. Carbon Dioxide Utilisation for Production of Transport Fuels: Process and Economic Analysis. *Energy Environ. Sci.* **2015**, *8*, 1775−1789.

(3) Ma, X.; Wang, X.; Song, C. "Molecular Basket" Sorbents for Separation of CO_2 and H_2S from Various Gas Streams. *J. Am. Chem. Soc.* **2009**, *131*, 5777−5783.

(4) Gnanamani, M. K.; Jacobs, G.; Hamdeh, H. H.; Shafer, W. D.; Liu, F.; Hopps, S. D.; Thomas, G. A.; Davis, B. H. Hydrogenation of Carbon Dioxide over Co-Fe Bimetallic Catalysts. *ACS Catal.* **2016**, *6*, 913−927.

(5) Riedel, T.; Claeys, M.; Schulz, H.; Schaub, G.; Nam, S.; Jun, K.; Choi, M.; Kishan, G.; Lee, K. Comparative Study of Fischer−Tropsch Synthesis with H_2/CO and H_2/CO_2 Syngas Using Fe- and Co-Based Catalysts. *Appl. Catal., A* **1999**, *186*, 201−213.

(6) Albrecht, M.; Rodemerck, U.; Schneider, M.; Bröring, M.; Baabe, D.; Kondratenko, E. V. Unexpectedly Efficient CO_2 Hydrogenation to Higher Hydrocarbons over Non-Doped Fe_2O_3. *Appl. Catal., B* **2017**, *204*, 119−126.

(7) Visconti, C. G.; Martinelli, M.; Falbo, L.; Infantes-Molina, A.; Lietti, L.; Forzatti, P.; Iaquaniello, G.; Palo, E.; Picutti, B.; Brignoli, F. CO_2 Hydrogenation to Lower Olefins on a High Surface Area K-Promoted Bulk Fe-Catalyst. *Appl. Catal., B* **2017**, *200*, 530−542.

(8) Landau, M. V.; Meiri, N.; Utsis, N.; Vidruk Nehemya, R.; Herskowitz, M. Conversion of CO_2, CO, and H_2 in CO_2 Hydrogenation to Fungible Liquid Fuels on Fe-Based Catalysts. *Ind. Eng. Chem. Res.* **2017**, *56*, 13334−13355.

(9) Janlamool, J.; Praserthdam, P.; Jongsomjit, B. Ti-Si Composite Oxide-Supported Cobalt Catalysts for CO_2 Hydrogenation. *J. Nat. Gas Chem.* **2011**, *20*, 558−564.

(10) Zhou, G.; Wu, T.; Xie, H.; Zheng, X. Effects of Structure on the Carbon Dioxide Methanation Performance of Co-Based Catalysts. *Int. J. Hydrogen Energy* **2013**, *38*, 10012−10018.

(11) Zhou, G.; Wu, T.; Zhang, H.; Xie, H.; Feng, Y. Carbon Dioxide Methanation on Ordered Mesoporous Co/KIT-6 Catalyst. *Chem. Eng. Commun.* **2014**, *201*, 233−240.

(12) Shin, H. H.; Lu, L.; Yang, Z.; Kiely, C. J.; McIntosh, S. Cobalt Catalysts Decorated with Platinum Atoms Supported on Barium Zirconate Provide Enhanced Activity and Selectivity for CO_2 Methanation. *ACS Catal.* **2016**, *6*, 2811−2818.

(13) Du, G.; Lim, S.; Yang, Y.; Wang, C.; Pfefferle, L.; Haller, G. Methanation of Carbon Dioxide on Ni-Incorporated MCM-41 Catalysts: The Influence of Catalyst Pretreatment and Study of Steady-State Reaction. *J. Catal.* **2007**, *249*, 370−379.

(14) Rossetti, I.; Biffi, C.; Bianchi, C. L.; Nichele, V.; Signoretto, M.; Menegazzo, F.; Finocchio, E.; Ramis, G.; Di Michele, A. Ni/SiO_2 and Ni/ZrO_2 Catalysts for the Steam Reforming of Ethanol. *Appl. Catal., B* **2012**, *117−118*, 384−396.

(15) Visconti, C. G.; Martinelli, M.; Falbo, L.; Fratalocchi, L.; Lietti, L. CO_2 Hydrogenation to Hydrocarbons over Co and Fe-Based Fischer−Tropsch Catalysts. *Catal. Today* **2016**, *277*, 161−170.

(16) Kattel, S.; Yu, W.; Yang, X.; Yan, B.; Huang, Y.; Wan, W.; Liu, P.; Chen, J. G. CO Hydrogenation over Oxide-Supported PtCo Catalysts: The Role of the Oxide Support in Determining the Product Selectivity. *Angew. Chem., Int. Ed.* **2016**, *55*, 7968−7973.

(17) Kim, A.; Sanchez, C.; Patriarche, G.; Ersen, O.; Moldovan, S.; Wisnet, A.; Sassoye, C.; Debecker, D. P. Selective CO_2 Methanation on Ru/TiO_2 Catalysts: Unravelling the Decisive Role of the TiO_2 Support Crystal Structure. *Catal. Sci. Technol.* **2016**, *6*, 8117−8128.

(18) Lin, Y.; Zhu, Y.; Pan, X.; Bao, X. Modulating the Methanation Activity of Ni by the Crystal Phase of TiO_2. *Catal. Sci. Technol.* **2017**, *7*, 2813−2818.

(19) Xu, J.; Su, X.; Duan, H.; Hou, B.; Lin, Q.; Liu, X.; Pan, X.; Pei, G.; Geng, H.; Huang, Y.; Zhang, T. Influence of Pretreatment Temperature on Catalytic Performance of Rutile TiO_2 -Supported

Ruthenium Catalyst in CO_2 Methanation. *J. Catal.* **2016**, *333*, 227–237.

(20) Satthawong, R.; Koizumi, N.; Song, C.; Prasassarakich, P. Light Olefin Synthesis from CO_2 Hydrogenation over K-Promoted Fe-Co Bimetallic Catalysts. *Catal. Today* **2015**, *251*, 34–40.

(21) Boreriboon, N.; Jiang, X.; Song, C.; Prasassarakich, P. Higher Hydrocarbons Synthesis from CO_2 Hydrogenation Over K- and La-Promoted Fe–Cu/TiO_2 Catalysts. *Top. Catal.* **2018**, *61*, 1551–1562.

(22) Shi, H.; Zeng, D.; Li, J.; Wang, W. A Melting-Like Process and the Local Structures During the Anatase-to-Rutile Transition. *Mater. Charact.* **2018**, *146*, 237–242.

(23) Chung, Y.; Xiong, G.; Kao, C. Mechanism of Strong Metal-Support Interaction in Ni/TiO_2. *J. Catal.* **1984**, *85*, 237–243.

(24) Andersson, M.; Lars, Ö.; Sten, L.; Anders, P. Preparation of Nanosize Anatase and Rutile TiO_2 by Hydrothermal Treatment of Microemulsions and Their Activity for Photocatalytic Wet Oxidation of Phenol. *J. Phys. Chem. B* **2002**, *106*, 10674–10679.

(25) Park, N.; van de Lagemat, J.; Frank, A. Comparison of Dye-Sensitized Rutile- and Anatase-Based TiO_2 Solar Cells. *J. Phys. Chem. B* **2000**, *104*, 8989–8994.

(26) Lee, J.; Burt, S. P.; Carrero, C. A.; Alba-Rubio, A. C.; Ro, I.; O'Neill, B. J.; Kim, H. J.; Jackson, D. H. K.; Kuech, T. F.; Hermans, I.; Dumesic, J. A.; Huber, G. W. Stabilizing Cobalt Catalysts for Aqueous-Phase Reactions by Strong Metal-Support Interaction. *J. Catal.* **2015**, *330*, 19–27.

(27) Levin, M.; Salmeron, M.; Bell, A.; Somorjai, G. The Effects of Titania and Alumina Overlayers on the Hydrogenation of CO over Rhodium. *J. Chem. Soc., Faraday Trans. 1* **1987**, *83*, 2061–2069.

(28) Bertella, F.; Concepción, P.; Martínez, A. TiO_2 Polymorph Dependent SMSI Effect in Co-Ru/TiO_2 Catalysts and Its Relevance to Fischer–Tropsch Synthesis. *Catal. Today* **2017**, *289*, 181–191.

(29) Liu, Y.; Fang, K.; Chen, J.; Sun, Y. Effect of Pore Size on the Performance of Mesoporous Zirconia-Supported Cobalt Fischer–Tropsch Catalysts. *Green Chem.* **2007**, *9*, 611–615.

(30) Wang, H.; Wang, M.; Zhang, W.; Zhao, N.; Wei, W.; Sun, Y. Synthesis of Dimethyl Carbonate from Propylene Carbonate and Methanol Using CaO-ZrO_2 Solid Solutions as Highly Stable Catalysts. *Catal. Today* **2006**, *115*, 107–110.

(31) Díez, V. K.; Apesteguía, C. R.; Di Cosimo, J. I. Acid-Base Properties and Active Site Requirements for Elimination Reactions on Alkali-Promoted MgO Catalysts. *Catal. Today* **2000**, *63*, 53–62.

(32) Zhong, C.; Guo, X.; Mao, D.; Wang, S.; Wu, G.; Lu, G. Effects of Alkaline-Earth Oxides on the Performance of a CuO-ZrO_2 Catalyst for Methanol Synthesis via CO_2 Hydrogenation. *RSC Adv.* **2015**, *5*, 52958–52965.

(33) Nie, X.; Wang, H.; Li, W.; Chen, Y.; Guo, X.; Song, C. DFT Insight into the Support Effect on the Adsorption and Activation of Key Species over Co Catalysts for CO_2 Methanation. *J. CO_2 Util.* **2018**, *24*, 99–111.

(34) Nie, X.; Wang, H.; Janik, M.; Chen, Y.; Guo, X.; Song, C. Mechanistic Insight Into C-C Coupling over Fe-Cu Bimetallic Catalysts in CO_2 Hydrogenation. *J. Phys. Chem. C* **2017**, *121*, 13164–13174.

(35) Chew, L. M.; Kangvansura, P.; Ruland, H.; Schulte, H. J.; Somsen, C.; Xia, W.; Eggeler, G.; Worayingyong, A.; Muhler, M. Effect of Nitrogen Doping on the Reducibility, Activity and Selectivity of Carbon Nanotube-Supported Iron Catalysts Applied in CO_2 Hydrogenation. *Appl. Catal., A* **2014**, *482*, 163–170.

(36) Kangvansura, P.; Chew, L. M.; Saengsui, W.; Santawaja, P.; Poo-arporn, Y.; Muhler, M.; Schulz, H.; Worayingyong, A. Product Distribution of CO_2 Hydrogenation by K- and Mn-Promoted Fe Catalysts Supported on N-Functionalized Carbon Nanotubes. *Catal. Today* **2016**, *275*, 59–65.

(37) Kattel, S.; Yan, B.; Yang, Y.; Chen, J. G.; Liu, P. Optimizing Binding Energies of Key Intermediates for CO_2 Hydrogenation to Methanol over Oxide-Supported Copper. *J. Am. Chem. Soc.* **2016**, *138*, 12440–12450.

(38) Kattel, S.; Yan, B.; Chen, J. G.; Liu, P. CO_2 Hydrogenation on Pt, Pt/SiO_2 and Pt/TiO_2: Importance of Synergy between Pt and Oxide Support. *J. Catal.* **2016**, *343*, 115–126.

(39) Yang, Y.; White, M. G.; Liu, P. Theoretical Study of Methanol Synthesis from CO_2 Hydrogenation on Metal-Doped Cu(111) Surfaces. *J. Phys. Chem. C* **2012**, *116*, 248–256.

(40) Zhu, J.; Yang, J.; Bian, Z.; Ren, J.; Liu, Y.; Cao, Y.; Li, H.; He, H.; Fan, K. Nanocrystalline Anatase TiO_2 Photocatalysts Prepared via a Facile Low Temperature Nonhydrolytic Sol-Gel Reaction of $TiCl_4$ and Benzyl Alcohol. *Appl. Catal., B* **2007**, *76*, 82–91.

(41) He, Z.; Que, W.; Chen, J.; He, Y.; Wang, G. Surface Chemical Analysis on the Carbon-Doped Mesoporous TiO_2 Photocatalysts After Post-Thermal Treatment: XPS and FTIR Characterization. *J. Phys. Chem. Solids* **2013**, *74*, 924–928.

(42) Bowker, M. The Surface Structure of Titania and the Effect of Reduction. *Curr. Opin. Solid State Mater. Sci.* **2006**, *10*, 153–162.

(43) Liu, X.; Wang, M.; Zhou, C.; Zhou, W.; Cheng, K.; Kang, J.; Zhang, Q.; Deng, W.; Wang, Y. Selective Transformation of Carbon Dioxide into Lower Olefins with a Bifunctional Catalyst Composed of $ZnGa_2O_4$ and SAPO-34. *Chem. Commun.* **2018**, *54*, 140–143.

(44) Gao, P.; Dang, S.; Li, S.; Bu, X.; Liu, Z.; Qiu, M.; Yang, C.; Wang, H.; Zhong, L.; Han, Y.; Liu, Q.; Wei, W.; Sun, Y. Direct Production of Lower Olefins from CO_2 Conversion via Bifunctional Catalysis. *ACS Catal.* **2018**, *8*, 571–578.

(45) Daturi, M.; Binet, C.; Lavalley, J. C.; Blanchard, G. Surface FTIR Investigations on $Ce_xZr_{1-x}O_2$ System. *Surf. Interface Anal.* **2000**, *30*, 273–277.

(46) Takano, H.; Kirihata, Y.; Izumiya, K.; Kumagai, N.; Habazaki, H.; Hashimoto, K. Highly Active Ni/Y-Doped ZrO_2 Catalysts for CO_2 Methanation. *Appl. Surf. Sci.* **2016**, *388*, 653–663.

(47) Gupta, N.; Kamble, V.; Kartha, V.; Iyer, R.; Thampi, K.; Gratzel, M. FTIR Spectroscopic Study of the Interaction of CO_2 and CO_2 + H_2 over Partially Oxidized Ru/TiO_2 Catalyst. *J. Catal.* **1994**, *146*, 173–184.

(48) Le Peltier, F.; Chaumette, P.; Saussey, J.; Bettahar, M.; Lavalley, J. In Situ FT-IR and Kinetic Study of Methanol Synthesis from CO_2/H_2 over $ZnAl_2O_4$ and Cu-$ZnAl_2O_4$ Catalysts. *J. Mol. Catal. A: Chem.* **1998**, *132*, 91–100.

(49) Bersani, M.; Gupta, K.; Mishra, A. K.; Lanza, R.; Taylor, S. F. R.; Islam, H.-U.; Hollingsworth, N.; Hardacre, C.; de Leeuw, N. H.; Darr, J. A. Combined EXAFS, XRD, DRIFTS, and DFT Study of Nano Copper-Based Catalysts for CO_2 Hydrogenation. *ACS Catal.* **2016**, *6*, 5823–5833.

(50) Zhu, Y.; Pan, X.; Jiao, F.; Li, J.; Yang, J.; Ding, M.; Han, Y.; Liu, Z.; Bao, X. Role of Manganese Oxide in Syngas Conversion to Light Olefins. *ACS Catal.* **2017**, *7*, 2800–2804.

(51) Jacobs, G.; Patterson, P. M.; Williams, L.; Chenu, E.; Sparks, D.; Thomas, G.; Davis, B. H. Water-Gas Shift: In Situ Spectroscopic Studies of Noble Metal Promoted Ceria Catalysts for CO Removal in Fuel Cell Reformers and Mechanistic Implications. *Appl. Catal., A* **2004**, *262*, 177–187.

(52) Pan, Q.; Peng, J.; Wang, S.; Wang, S. In Situ FTIR Spectroscopic Study of the CO_2 Methanation Mechanism on Ni/$Ce_{0.5}Zr_{0.5}O_2$. *Catal. Sci. Technol.* **2014**, *4*, 502–509.

(53) Wang, F.; He, S.; Chen, H.; Wang, B.; Zheng, L.; Wei, M.; Evans, D. G.; Duan, X. Active Site Dependent Reaction Mechanism over Ru/CeO_2 Catalyst toward CO_2 Methanation. *J. Am. Chem. Soc.* **2016**, *138*, 6298–6305.

(54) Zhou, G.; Liu, H.; Cui, K.; Jia, A.; Hu, G.; Jiao, Z.; Liu, Y.; Zhang, X. Role of Surface Ni and Ce Species of Ni/CeO_2 Catalyst in CO_2 Methanation. *Appl. Surf. Sci.* **2016**, *383*, 248–252.

(55) Solis-Garcia, A.; Louvier-Hernandez, J. F.; Almendarez-Camarillo, A.; Fierro-Gonzalez, J. C. Participation of Surface Bicarbonate, Formate and Methoxy Species in the Carbon Dioxide Methanation Catalyzed by ZrO_2-Supported Ni. *Appl. Catal., B* **2017**, *218*, 611–620.

(56) Schild, C.; Wokaun, A.; Baiker, A. On the Hydrogenation of CO and CO_2 over Copper/Zirconia and Palladium/Zirconia Catalysts. *Fresenius' J. Anal. Chem.* **1991**, *341*, 395–401.

(57) Li, W.; Nie, X.; Jiang, X.; Zhang, A.; Ding, F.; Liu, M.; Liu, Z.; Guo, X.; Song, C. ZrO_2 Support Imparts Superior Activity and Stability of Co Catalysts for CO_2 Methanation. *Appl. Catal., B* **2018**, *220*, 397−408.

(58) Johnson, G. R.; Bell, A. T. Role of ZrO_2 in Promoting the Activity and Selectivity of Co-Based Fischer−Tropsch Synthesis Catalysts. *ACS Catal.* **2016**, *6*, 100−114.

(59) Satthawong, R.; Koizumi, N.; Song, C.; Prasassarakich, P. Bimetallic Fe-Co Catalysts for CO_2 Hydrogenation to Higher Hydrocarbons. *J. CO_2 Util.* **2013**, *3−4*, 102−106.

(60) Li, W.; Huang, H.; Li, H.; Zhang, W.; Liu, H. Facile Synthesis of Pure Monoclinic and Tetragonal Zirconia Nanoparticles and Their Phase Effects on the Behavior of Supported Molybdena Catalysts for Methanol-Selective Oxidation. *Langmuir* **2008**, *24*, 8358−8366.